On linear and nonlinear aspects of dynamic mode decomposition

A. K. Alekseev[1], D. A. Bistrian[2], A. E. Bondarev[3] and I. M. Navon[4],*,†

[1]*Moscow Institute of Physics and Technology, Moscow, Russia*
[2]*Department of Electrical Engineering and Industrial Informatics, Politehnica University of Timişoara, 331128, Hunedoara, Romania*
[3]*Keldysh Institute of Applied Mathematics RAS, Moscow, Russia*
[4]*Department of Scientific Computing, Florida State University, Tallahassee, FL 32306-4120, USA*

SUMMARY

The approximation of reduced linear evolution operator (propagator) via dynamic mode decomposition (DMD) is addressed for both linear and nonlinear events. The 2D unsteady supersonic underexpanded jet, impinging the flat plate in nonlinear oscillating mode, is used as the first test problem for both modes. Large memory savings for the propagator approximation are demonstrated. Corresponding prospects for the estimation of receptivity and singular vectors are discussed. The shallow water equations are used as the second large-scale test problem. Excellent results are obtained for the proposed optimized DMD method of the shallow water equations when compared with recent POD-based/discrete empirical interpolation-based model reduction results in the literature. Copyright © 2016 John Wiley & Sons, Ltd.

1. INTRODUCTION

The dynamic mode decomposition (DMD) is a recently devised method for the search of a small number of basis vectors (dynamic modes) able to describe the total fluid state [1–12]. It promises certain advance in the retrieval of flow structures, which provide a low-dimensional approximation of complex unsteady flowfields. DMD is based on an algorithm for numerical estimation of eigenvalues Λ and right eigenvectors Ω_R of an operator A determining the flow evolution (linear propagator). The set of flow snapshots is used as the input data.

A powerful way of analyzing nonlinear flow dynamics using linear techniques is provided by the use of dynamic modes (e.g., the work of Holmes *et al.* [7], Bagheri [8], and Mezic [9]). Among several snapshot-based modal decomposition methods, DMD has been widely applied to study the physics of the dynamics of the flows in different applications.

A related theoretical framework is proposed by Tu *et al.* [10], in which DMD is defined as the eigendecomposition of an approximating linear operator. They demonstrate the utility of this approach by presenting novel sampling strategies that increase computational efficiency and mitigate the effects of noise. A new technique that allows dynamical information to be extracted from large datasets and data streams is proposed by Hemati *et al.* [11]. Their low-storage method for performing DMD can be updated inexpensively as new data become available. The problem of modal decomposition of large and arbitrarily sampled systems is addressed by Guéniat *et al.* [4].

---

*Correspondence to: I. M. Navon, Department of Scientific Computing, Florida State University, Tallahassee, FL 32306–4120, USA.
†E-mail: inavon@fsu.edu

Their method essentially formulates the problem in an optimization setting and decouples the estimation of the temporal description from the spatial description.

In a bold manner, the problem of systems governed by nonlinear evolution laws is addressed by Williams and his coworkers [12]. They demonstrate that the Koopman eigenfunctions and eigenvalues define a set of intrinsic coordinates, which serve as a natural framework for fusing measurements obtained from heterogeneous collections of sensors.

In the present paper, we denote the operator A as the Schmid operator (which acts on dynamic variables) in order to distinguish it from the Koopman operator [2, 13, 14] (which acts on observable variables).

The DMD approach enables one to obtain also a set of left eigenvectors Ω_L. This set provides the feasibility to approximate the reduced form Schmid operator as a product of the diagonal and two rectangular matrices $A_r = \Omega_R \Lambda \Omega_L$. In this form, the approximation of the Schmid operator A may be efficiently stored and used implicitly.

The matrix form of Schmid operator A is interesting for several important classes of problems. For example, the adjoint propagator $A*$ is used in receptivity problems [15]. The actions of the operator $A*A$ are used for the maximal eigenvalue estimation. The corresponding eigenvector provides the most rapidly growing perturbations at a finite time interval (singular vectors [16]) that are also of current interest.

Both the evaluation of receptivity and the estimation of the singular vectors are linear problems. If flow dynamics are nonlinear, the linear approximation of the operator A may be based on a linear-tangent approximation that requires additional coding. However, because temporal steps of the finite volume algorithm may be chosen as small as necessary, a linear-tangent approximation may be avoided for a short-time interval (several temporal steps) between snapshots.

Dynamic mode decomposition also may be applied to essentially nonlinear problems [2]. The physical meaning of the operator changes for longer time intervals (thus providing nonlinearity); at some limit, the operator may become independent of the snapshots selection and may be considered as a form of the Koopman operator.

The paper aims to investigate the properties and applications of the DMD in the form of reduced Schmid operator. This form provides a high computational efficiency as well as a straightforward adaptation to several important domains of application.

The remainder of this article is organized as follows. In Section 2, we present one of the main versions of DMD in accordance with [1] along with some of its properties especially useful for our purposes. Section 3 considers the construction of the Schmid operator as a product of rectangular matrices and the equivalence of DMD and Schmid operator. Section 4 analyzes the relations between the Schmid operator and the propagator (flow evolution operator) in both linear and nonlinear modes. Further, in Section 5, the numerical test results of the Schmid operator estimation in linear and nonlinear modes are presented. A supersonic jet interaction with the flat surface is considered as one of the illustrative test problems. The second test problem addresses flows described by shallow water equations. Several problems, having applications for the Schmid operator applications, are surveyed in Section 6. Conclusions are drawn and presented in Section 7.

2. DMD VERSION FOR NON-NORMALIZED MODES

There exist several approaches to DMD construction that include normalized dynamic modes [1], non-normalized dynamic modes [2, 6], and optimization over eigenvalues [3, 4]. In the present paper, it is more convenient from our purposes to use normalized modes. So, herein, we consider the main features of DMD in accordance with [1] (the present section exposition is very close to [1] because of need for further analysis lucidity).

Let us consider a set of N snapshots $Sn_1^N = (u_1, \ldots, u_N)$, which are discrete approximations of the flow fields at consecutive time instances separated by an identical interval Δt. Each snapshot u_i is a vector of the dimension Nt. The linear operator $A(\Delta t)$ (an unknown matrix of dimension $Nt \times Nt$) is assumed to exist and provide the transformation $u_{i+1} = Au_i$. In this case, the snapshots form a Krylov sequence $Sn_1^N = \{u_1, Au_1, A^2 u_1, \ldots, A^{N-1} u_1\}$.

For a long enough snapshot set, the eigenvalues and right eigenvectors $Av_j = \lambda_j v_j$ may be calculated, and the snapshots may be written as

$$u_k = \sum_j a_j v_j \lambda^{k-1} = \sum_j a_j v_j e^{(\sigma_j + i\omega_j)(k-1)\Delta t}, \quad (k = 1, N). \tag{1}$$

Usually, the right eigenvectors $v_j \in C$ are denoted as dynamic (Koopman) modes, the eigenvalues $\lambda_j \in C$ are denoted as (Koopman) eigenvalues, and the coefficients $a_i \in C$ are denoted as amplitudes (Koopman eigenfunctions).

The estimation of Koopman modes, eigenvalues, and amplitudes from the known set of snapshots Sn_1^N is the main computational problem from this viewpoint. The sets of shifted snapshots $Sn_1^{N-1} = (u_1, \dots, u_{N-1}) = (u_1, \dots, A^{N-2}u_1)$, $Sn_2^N = (u_2, \dots, u_N) = ASn_1^{N-1}$ are used, herein, according to [1]. The set Sn_1^N is assumed to capture the main physical features of a considered process more precisely as the number of snapshots increases. If a certain critical number of snapshots exceeded, the following snapshots should become linearly dependent on the previous ones (similar to Krylov-type iteration processes). In this limit, the last snapshot u_N may be expressed via the previous snapshots with some error r:

$$u_N = c_1 u_1 + c_2 u_2 + \dots + c_{N-1} u_{N-1} + r. \tag{2}$$

By substituting u_N in Sn_2^N and using a companion matrix C, we obtain $Sn_2^N = Sn_1^{N-1} \cdot C + r$, where

$$C = \begin{pmatrix} 0 & & & & c_1 \\ 1 & 0 & & & c_2 \\ & 1 & 0 & & \\ & & \dots & \dots & \\ & & & 1 & c_{N-1} \end{pmatrix}. \tag{3}$$

The expression $Sn_2^N \approx Sn_1^{N-1} \cdot C$ holds under the assumption of small r. Thus, it can be stated that

$$A \cdot Sn_1^{N-1} = Sn_2^N = Sn_1^{N-1} \cdot C. \tag{4}$$

The set of snapshots may be presented using SVD [17] as follows:

$$Sn_1^{N-1} = U\Sigma V^*. \tag{5}$$

Because the snapshot matrix is not invertible, the Moore–Penrose pseudoinverse matrix for Sn_1^{N-1} is used, which can be written as $V\Sigma^+ U^*$. We denote here $\Sigma^+ = diag\left(\sigma_1^{-1}, \dots, \sigma_r^{-1}, 0, \dots, 0\right)$. From the expression $Sn_2^N = Sn_1^{N-1}C$, one may obtain via the pseudoinverse matrix

$$C = V\Sigma^+ U^* Sn_2^N. \tag{6}$$

Let us change the companion matrix C by the transformation

$$\widetilde{C} = (V\Sigma^+)^{-1} C (V\Sigma^+). \tag{7}$$

Under this transformation, eigenvalues do not change, while the eigenvectors are rotated:

$$y^C = V\Sigma^+ y^{\widetilde{C}}, \quad y^{\widetilde{C}} = \Sigma V^* y^C.$$

Further, the substitution of expression (6) into (7) yields

$$\widetilde{C} = U^* Sn_2^N V\Sigma^+. \tag{8}$$

From $A \cdot Sn_1^{N-1} = Sn_1^{N-1} \cdot C$, one may obtain $A \cdot U\Sigma V^* = U\Sigma V^* \cdot C$, $A \cdot U = U\Sigma V^* \cdot C \cdot (\Sigma V^*)^{-1}$, and $A \cdot U = U\widetilde{C}$. Taking into account $\widetilde{C} = W\Lambda W^{-1}$ ($W = \Omega_R^{\widetilde{C}}$), we obtain the expression

$$A \cdot UW = UW \cdot \Lambda. \tag{9}$$

One can see from (9) that the eigenvalues Λ of the matrix $\widetilde{C}$ coincide with the eigenvalues of A. The right eigenvector of A assumes the form:

$$\Omega_R^A = UW = U\Omega_R^{\widetilde{C}}. \tag{10}$$

Because the matrix C is not symmetric, the right eigenvectors do not form an orthogonal basis, and the set of left eigenvectors (biorthogonal to right) is necessary. They may be obtained from the expression $A \cdot Sn_1^{N-1} = Sn_1^{N-1} \cdot C$ via SVD decomposition of the snapshot set $A \cdot U\Sigma V^* = U\Sigma V^* \cdot C$. Further, the chain of transformations $V\Sigma^+ U^* \cdot A \cdot U\Sigma V^* = C$ $V\Sigma^+ U^* \cdot A = C \cdot V\Sigma^+ U^*$ provides the expression $U^* \cdot A = (V\Sigma^+)^{-1} \cdot C \cdot V\Sigma^+ U^* = \widetilde{C} U^*$. Taking into account the $\widetilde{C}$ eigenvector decomposition, we get $U^* \cdot A = W\Lambda W^{-1} U^*$ and obtain $W^{-1} U^* \cdot A = \Lambda W^{-1} U^*$ that determines the left eigenvector of A:

$$\Omega_L^A = W^{-1} U^* = \Omega_L^{\widetilde{C}} U^*. \tag{11}$$

This enables an expansion in the series over the right eigenvectors ($u_1 = a_j v_j$). The coefficients a_j may be calculated via the biorthogonality relation (l_i is the left eigenvector that belongs to Ω_L^A matrix)

$$v_k l_i^* = \delta_{ik} \tag{12}$$

and has the form

$$a_k = (l_k^* u). \tag{13}$$

3. THE REDUCED FORM OF THE SCHMID OPERATOR

Thus, the eigenvalues and (right and left) eigenvectors of the Schmid operator A may be estimated from the spectrum of the matrix $\widetilde{C} = U^* Sn_2^N V\Sigma^+$. Then, the construction of the Schmid operator in the following reduced form is feasible:

$$A_r = \Omega_R^A \Lambda \Omega_L^A, \tag{14}$$

where Ω_R^A, Ω_L^A are rectangular matrices and the matrix Λ is a diagonal one.

The explicit form of propagator matrix A requires very high memory of dimension about $Nt \times Nt$ for CFD applications. Even for moderate grids (for example, about 100 nodes over a single spatial coordinate) $Nt \sim 4 \times 10^4$ in the 2D case and $Nt \sim 5 \times 10^6$ in 3D case. The decomposition of A via a product of reduced matrices requires the storage of only $2Nt \times N + N$ numbers. In the 2D case for $Nt \sim 4 \times 10^4$ and $N \sim 40$, the memory saving is about three orders of magnitude. The CPU time savings are close or more significant because of the nonlinear growth of the computer time necessary for the spectrum estimation as the matrix order increases.

4. RELATIONS OF SCHMID OPERATOR AND PROPAGATOR

Let the dynamics of a system be described by the equation

$$du/dt = Bu. \tag{15}$$

This equation may be discretized by a finite volume method with a time step τ in the form $u_{n+1} = (E + B\tau) \cdot u_n$. In the analysis, we use M steps of evolution between consecutive snapshots u_k, u_{k+1}. Then, the time interval (sampling period) between snapshots is $M\tau = \Delta t$. The DMD results are highly sensitive to the value of Δt.

Herein. we consider two cases: the linear limit for small Δt that may be provided either by a small M (or by decreasing τ if necessary) and the standard DMD with significantly greater Δt (i.e., nonlinear limit). The validity of Δt selection in the linear limit may be easily checked, while the optimal choice of Δt in nonlinear limit is rather nontransparent and requires laborious analysis (for example, the method fails when Δt is close to the main period of oscillation).

Consider an approximation of the solution propagator and its relations with the Schmid operator for both linear and nonlinear events. The linear case If an operator B does not depend on u, then the propagator approximation may be written as a product of the single time step τ operators

$$L(\Delta t)u_1 = e^{\sum B\tau}u_1 = e^{\sum B\Delta t/M}u_1 = e^{B\Delta t}u_1 = A(\Delta t)u_1. \tag{16}$$

So, in the linear case, the Schmid operator is equivalent to the approximation of the propagator $L(\Delta t) = A(\Delta t)$. The nonlinear case In general, an approximation of the nonlinear propagator assumes the form

$$L(\Delta t)u_1 = (E + B_1\tau)\cdot(E + B_2\tau)\ldots(E + B_M\tau)u_1 \tag{17}$$

Here, $u_n, u_2^*, \ldots, u_M^*, u_{n+1}$ are intermediate points between snapshots u_n and u_{n+1}, $B_i = B\left(u_i^*\right)$. Expression (17) essentially depends on the set of points between snapshots and, thus, is not invariant for different intervals. Under this situation, the propagator approximation $L(\Delta t)$ does not correspond to the Schmid operator properties.

However, if by some reason, $L(\Delta t)$ is constant for all intervals between snapshots (for example, there exists an averaged over $B\left(u_i^*\right)$ operator $L(\Delta t)$), then the Schmid operator A may be considered as a propagator approximation.

In this event, there exists a matrix function $\Omega(\Delta t)$, such that

$$L(\Delta t) = e^{\Omega(\Delta t)} \tag{18}$$

Because $\Omega(\Delta t)$ may be constructed as a Magnus series $\Omega(\Delta t) = \sum_1^{\infty}\Omega_k(\Delta t)$ [18–20], the expression $\Omega = \ln A_r$ may serve as a way for the numerical approximation of the Magnus series.

Hence, there are two cases: linear and nonlinear ('averaged'), when such linear operator A may exist.

In the linear event, the operator A is estimated in vicinity of a single point of the dynamic system trajectory and implies a usual linearization.

For the nonlinear asymptotic, the operator A is defined on a large part of the system trajectory and implies a 'linearization in the large' in terms of [14]. This 'linearization' is closely related with the properties of the linear Koopman operator that is the adjoint of Perron–Frobenius operator (the propagator for linear Liouville equation). This subject is far above the scope of the present paper; the additional information may be found in [2, 9, 10, 14, 21].

5. NUMERICAL TESTS

Two large-scale problems are used for the demonstration of the aforementioned features of the reduced form of the Schmid operator approximation. The first problem concerns an unsteady flow of impinging jet described by the Euler equations. The second problem concerns flows described by the shallow water equations. Some numerical results are provided in the succeeding discussion.

5.1.1. 2D jet impingement simulation.   The subroutines DGESVD (LAPACK [22]) (Univ of Tennessee, Knoxville, TN, USA) and SNAUPD, SNEUPD (ARPACK [23]) (Rice University, Houston, Texas, USA) were used for SVD decomposition.

Subroutine DGEEV (LAPACK) (Univ of Tennessee, Knoxville, TN, USA) was used for the calculation of complex eigenvalues, right and left eigenvectors of the non-symmetric companion type matrices.

The numerical tests were conducted both for the low-dimensional problems with *a priori* known matrix operator A and for a large-scale problem for the Schmid operator computed from N snapshots, obtained from the numerical solution of the 2D Euler equations.

The original operator A was estimated from the set of its actions for low-dimensional operators (from 5×5 to 10×10). Results of numerical tests confirmed the correct reconstruction of the original operator A.

For a large-scale problem, the Schmid operator was reconstructed via the product of the rectangular matrices $Nt \times N$, where $Nt = 36000$ and $N = 10 \div 50$.

At a normal impingement of supersonic underexpanded jet on a plate, the flow pattern depends on parameters such as the Mach number M_a, pressure ratio $n = p_j/p_a$, and distance from nozzle exit by the surface x/d_a. Within a rather narrow range of parameters, oscillating flow modes are known to occur. In this mode, the shock wave structure causes peripheral pressure maximums, which may lead to an unsteady separation. The results of computation of the oscillating flow seem to be appropriate as a test problem in order to test performance of DMD. Evidently, the influence of turbulence is neglected. However, the shock-induced unsteady separation bubble may be successfully modeled by an inviscid numerical method providing a good agreement with the experimental data [24]. So, this model correctly represents a true nonlinear unsteady flow dynamics and is useful for DMD tests because of its low computational cost requirements. The following 2D+1 Euler equations are used.

$$\frac{\partial \rho}{\partial t} + \frac{\partial (\rho U_k)}{\partial x^k} = 0, \tag{19}$$

$$\frac{\partial (\rho U_i)}{\partial t} + \frac{\partial (\rho U_k U_i + P\delta_{ik})}{\partial x^k} = 0, \tag{20}$$

$$\frac{\partial (\rho E)}{\partial t} + \frac{\partial (\rho U_k h_0)}{\partial x^k} = 0. \tag{21}$$

Here, $U_i = (U, V)$ are the velocity components, $h_0 = (U^2 + V^2)/2 + h$, $h = \frac{\gamma}{\gamma-1}\frac{P}{\rho} = \gamma e$, $e = \frac{RT}{\gamma-1}$, and $E = (e + (U^2 + V^2)/2)$ are enthalpies and energies (per unit volume), respectively, and $P = \rho RT$ is the state equation.

The computations are performed in the spatial domain $\Omega = (0 < x < X_{\max}, 0 < y < Y_{\max})$ during the time interval $(0 < t < t_f)$ with the flow snapshot recorded at equally spaced time subintervals Δt.

At the boundary $(x = 0)$, we impose the supersonic inflow conditions, corresponding to a nozzle exit section and the environment conditions (pressure, temperature and zero normal derivatives of velocities) on another part of the boundary. At the right boundary, a no-penetration condition is set. On the lateral boundaries $(y = 0, y = Y_{\max})$, we impose the outflow conditions in the supersonic region and environment conditions at the subsonic part of the boundary.

The Euler equations were solved by a discretization method of second-order spatial accuracy [25] with the numerical fluxes calculated via the method by Sun and Katayama [26] and a second-order time discretization. The numerical results are obtained and used in further analysis in a dimensionless form, using the jet parameters (ρ_j, U_j, E_j, d_a) for the non-dimensionalization.

5.1.2. The gas dynamics features of the flow.   The periodic formation and disappearance of a separation bubble is specific for this mode. Figures 1 and 2 demonstrate the density fields for the maximal and minimal (developed separation bubble) pressure and corresponding streamlines.

The flow of the jet is directed along X axis and is retarded at wall (right boundary) past the shock wave. The density contours reflect the compression at the wall. Streamlines demonstrate the spreading of jet in Figure 1 and significant separation bubbles in Figure 2. The switching between these two modes is the reason for pressure oscillations.

Figure 3 provides the surface pressure variation in time at the axis of symmetry for the transitional and following oscillation modes. The results correspond to the flow parameters $M_a = 4.0$, $\gamma = 1.4$, $x/d_a = 15$, and $n = 4$. The pressure is non-dimensionalized by the jet parameters as $p = p^*/\left(\rho_j (U_j)_j^2\right)$, where asterisks denote a dimensional parameter.
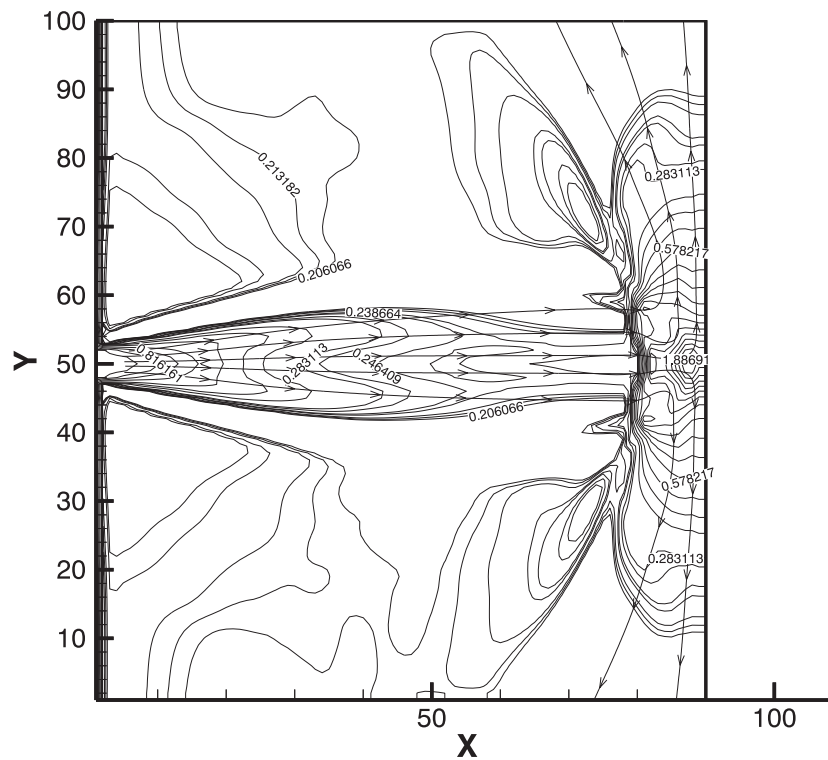
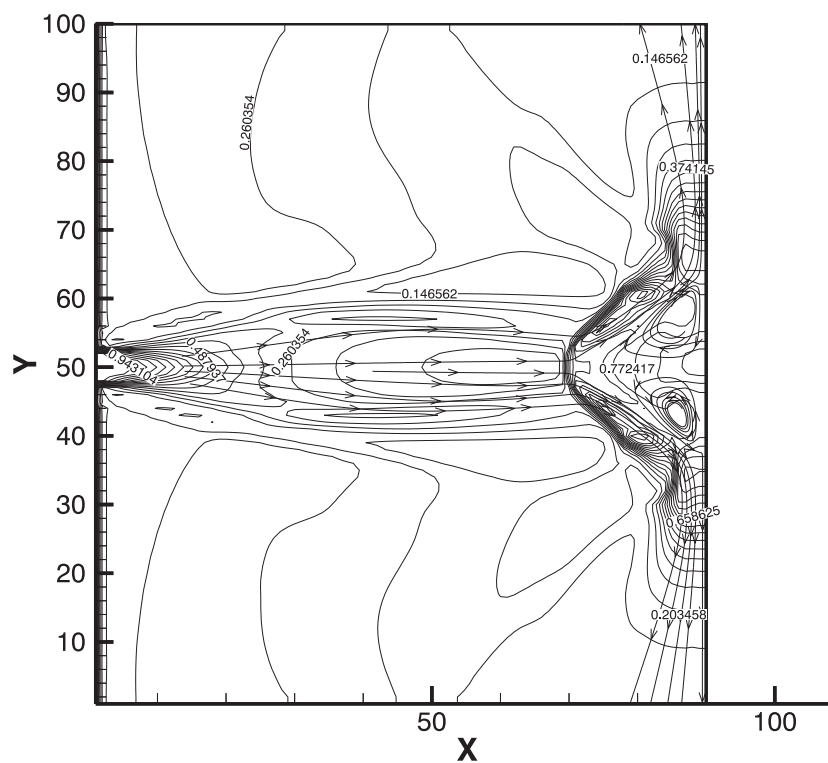Figure 1. Density isolines and streamlines for the maximal pressure.

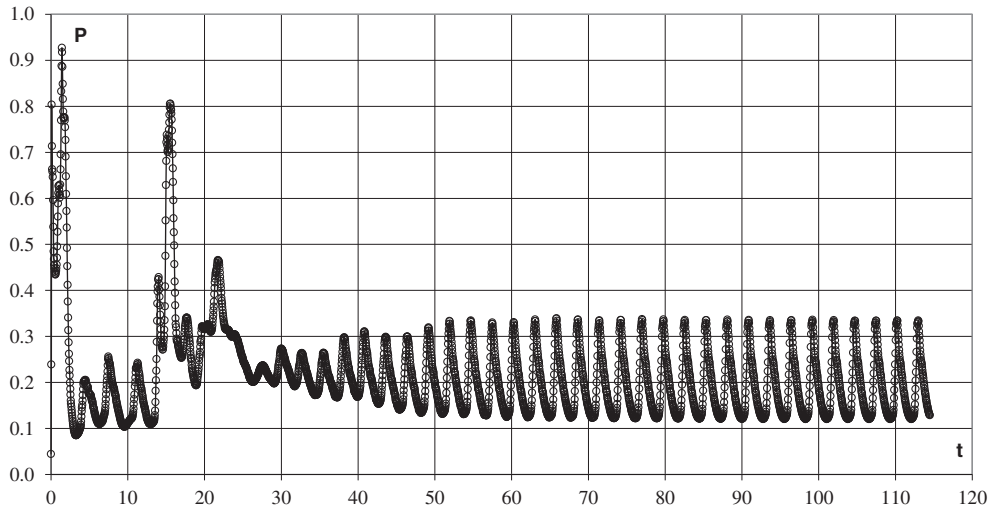Figure 2. Density isolines and streamlines for the minimal pressure.

Figure 3. The dimensionless pressure at the axis of symmetry as a function of dimensionless time.

5.1.3. DMD analysis for linear mode.   The existence of a linear mode is expected for a small interval Δt between the snapshots (several steps of the finite difference algorithm). The eigenvalues for linear problems, usually, are not located on the unit circle. Figure 4 presents the complex eigenvalues (dependence $\lambda_{Re}(\lambda_{Im})$) for the linear mode of evolution. The interval between snapshots is $\Delta t = 5\tau$ (τ is the step of finite-volume algorithm). The data are selected on the oscillations phase of the flow. The small Δt is chosen to ensure the study of the linear mode, and 15 snapshots are used.

Figures 5 and 6 illustrate the right real eigenvectors $\Omega_{R,1}$ (the component of density) for $\Delta t = k \cdot \tau$ ($k = 5$ and 10 steps of finite volume CFD algorithm). One may see a relatively small variation of the eigenvector structure at the time shift.

For $\Delta t = k \cdot \tau$ ($k = 5, 10$), Figures 7 and 8 depict amplitudes $Amp(\Omega_{R,4})$ (also density component) for one of the right complex eigenvectors $v_k = Amp_k e^{i\phi_k}$.

The variation of some eigenvalues as a function of the distance between the snapshots (number of time steps k) is provided in Figure 9. The eigenvalues are displayed for two real modes (lines 2 and 3). The phase shift α_4 is plotted for one of the complex modes (line 1). A linear dependence on k may be observed. The spectrum structure for the linear event is found to be stable that raises some questions,
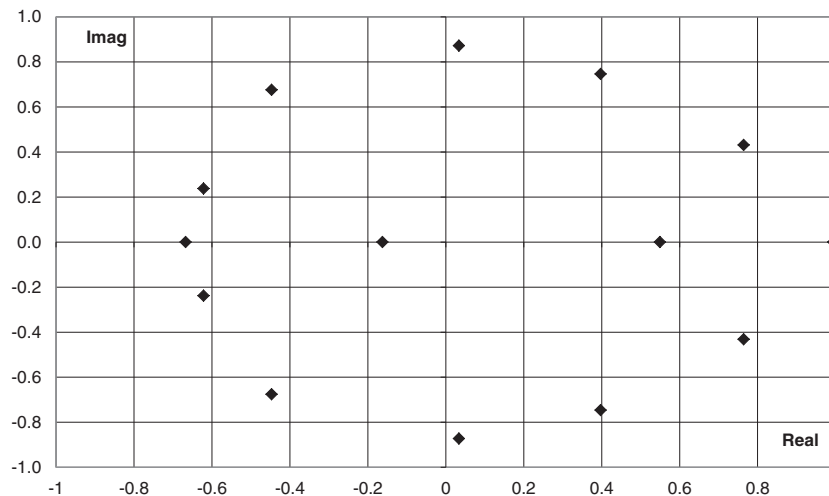

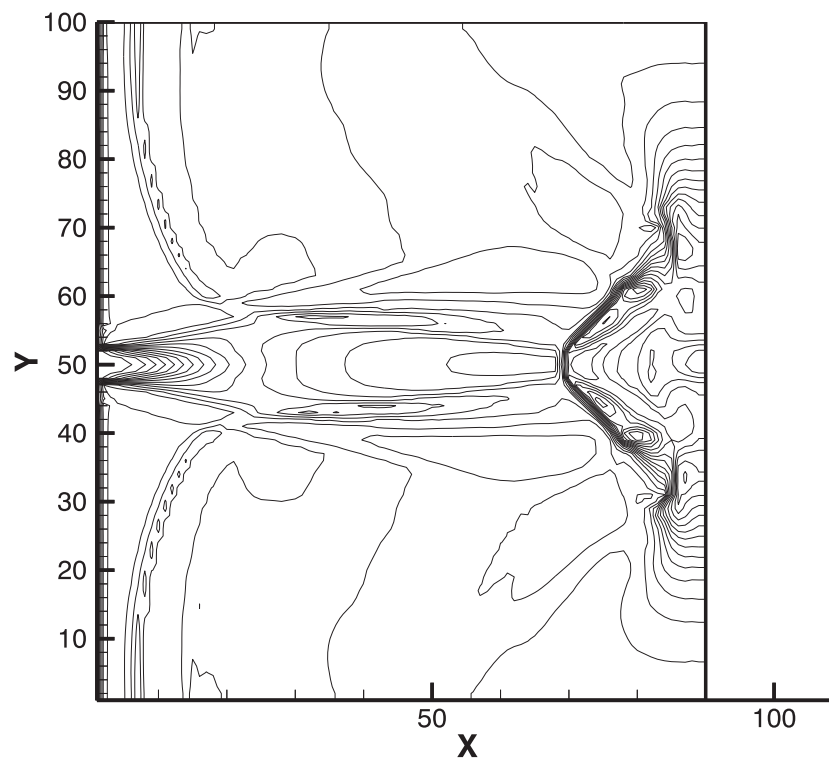Figure 4. Eigenvalues $\lambda_{Re}(\lambda_{Im})$.

Figure 5. Isolines of right real eigenvector $\Omega_{R,1}$ for $k=5$.
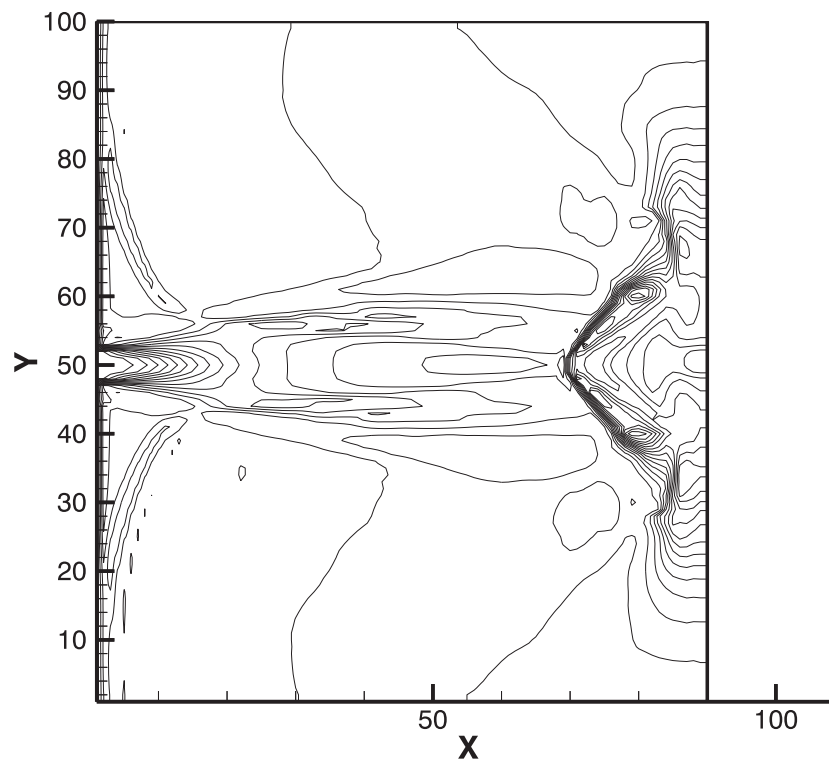

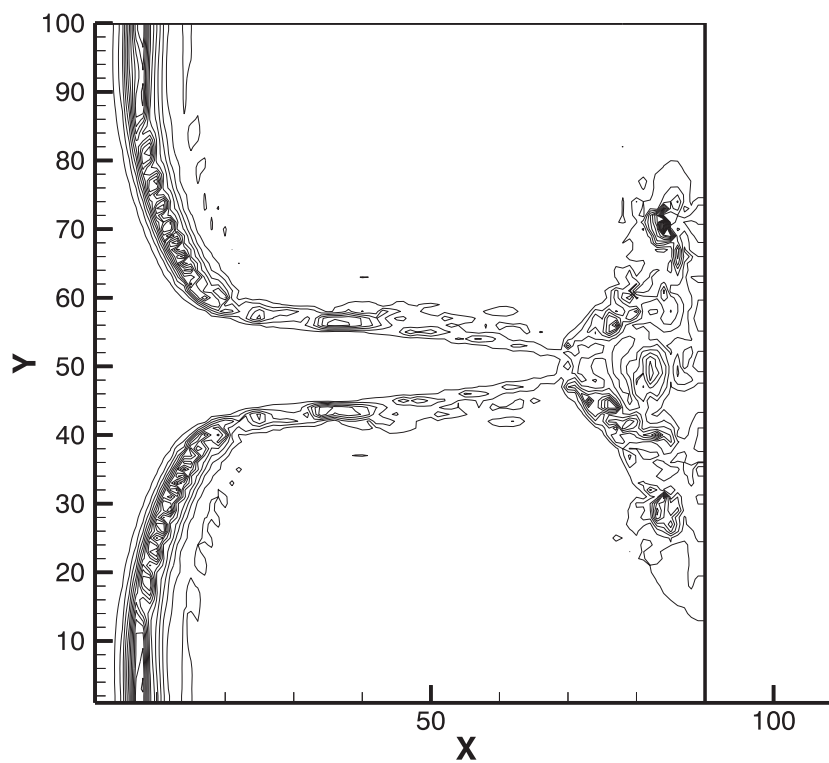Figure 6. Isolines of right real eigenvector $\Omega_{R,1}$ for $k=10$.

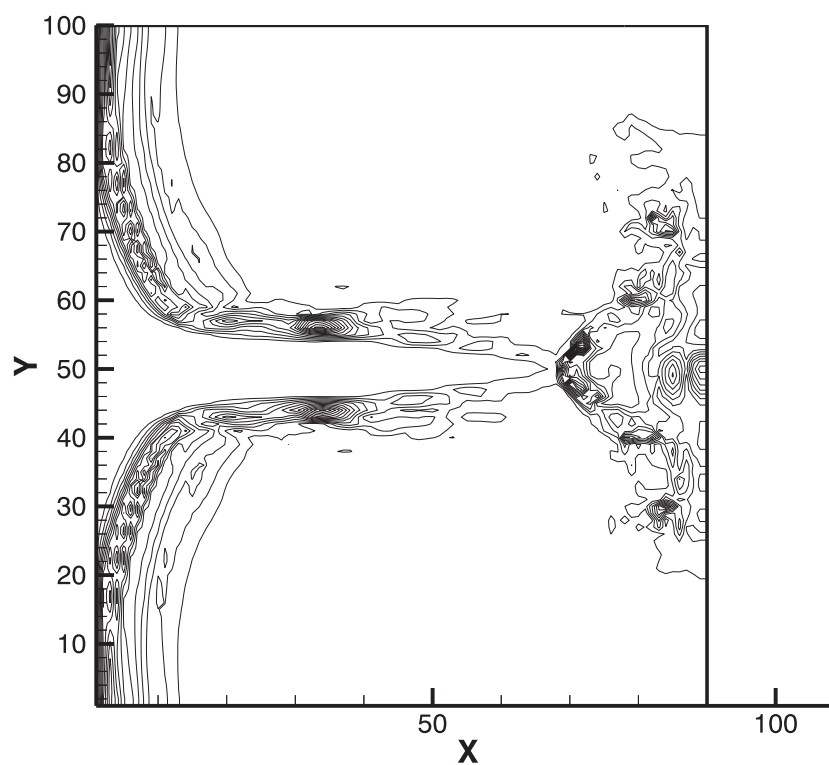Figure 7. Isolines of right complex eigenvector amplitude $Amp(\Omega_{R,4})$ for $k = 5$.

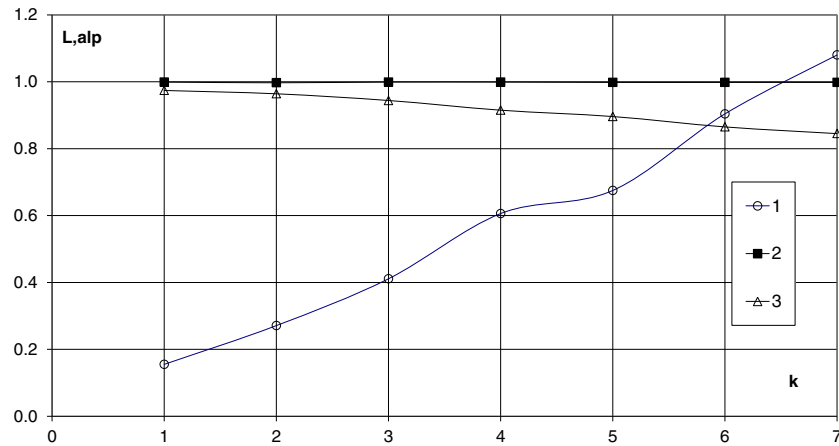Figure 8. Isolines of right complex eigenvector amplitude $Amp(\Omega_{R,4})$ for $k = 10$.

Figure 9. The real eigenvalues and the phase shift α_4 as functions of the number of time steps k. The number '1' is the phase shift α_4; '2' and '3' are two real eigenvalues.

because the visible evolution of the flow implies a significant movement in the state space. The reason may be the numerical error in eigenvalues that are close to the unit by module.

A comparison of the numerical results presented in Figures 5 to 8 demonstrates a relatively small variation of right eigenvectors Ω_R over k; a similar behavior is also specific for the left eigenvectors Ω_L. Thus, for the linear approach (at small distances Δt), the dynamics is determined by the variation of $\Lambda(\Delta t)$ at constants Ω_R and Ω_L. The evolution of flow, in this event, is caused by the rotation of constant eigenvectors in the complex plane.

At small intervals between snapshots (about single computation step), some ripples are visible in Ω_R and Ω_L. For $k \geq 5$, these ripples are practically invisible.

5.1.4. DMD analysis for nonlinear mode. Herein, only the self-oscillating part of the flow history is used for tests, because of its transparency. Figure 10 presents the dependence $\lambda_{Re}(\lambda_{Im})$ for time interval $\Delta t = 500$ steps, which far deviates from the oscillation period ($T_{osc} \approx 780$ steps). In this test, 40 snapshots are used. Eigenvalues are close to the unit circle that is common for nonlinear problems.

The spectrum structure for the nonlinear event seems visually to be stable that is quite natural for the stable attractor in the state space visible in Figure 3. However, the modules of several modes are slightly greater than the unit, a fact that may be caused by numerical errors.
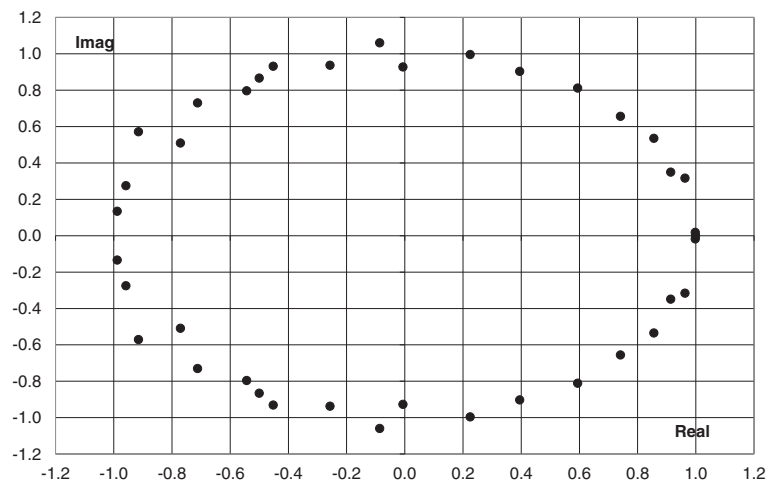

Figure 10. Eigenvalues $\lambda_{Re}(\lambda_{Im})$ for nonlinear mode.

Figure 11 shows the dependence of the amplitude on the frequency for 10 (line 1) and 40 (line 2) snapshots. The maximal amplitude correlates with the main frequency of oscillating mode ($\omega \approx 2.3$). Thus, DMD in nonlinear mode enables the capture of the main features of flow with highly nonlinear (because of shock waves) oscillations.

The quality of snapshot reconstruction may be estimated from Figures 12 and 13. Figure 12 represents one of the snapshots (density field at separation stage, $k = 800$), and Figure 13 represents the result of the reconstruction at $k = 800$ performed using the rotation of eigenvectors obtained from data at $k = 760$.
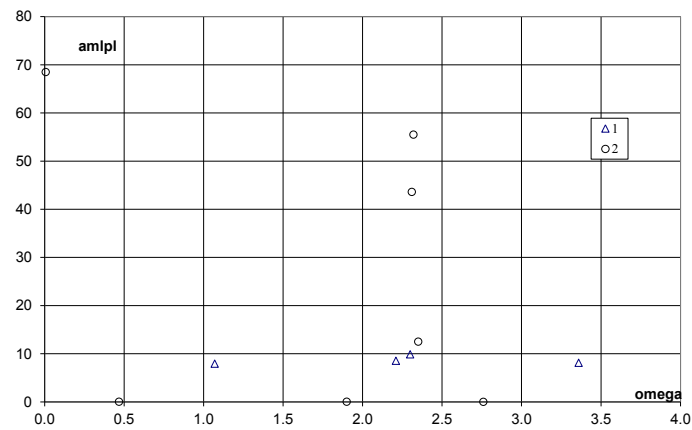

Figure 11. Amplitudes as a function of the optimal frequency estimations. The number '1' corresponds to 10 snapshots; '2' corresponds to 40 snapshots.
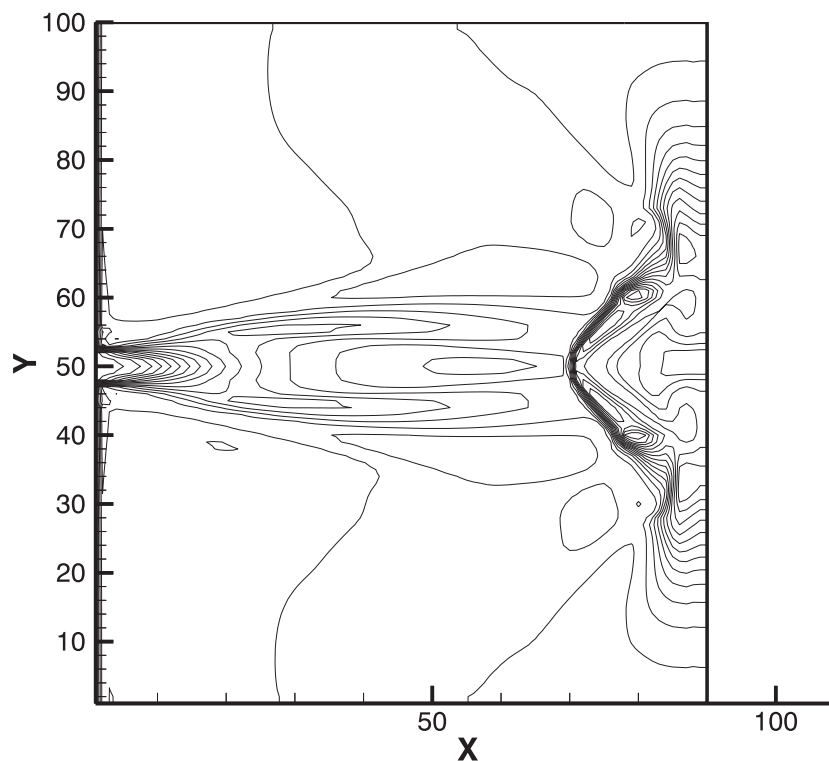

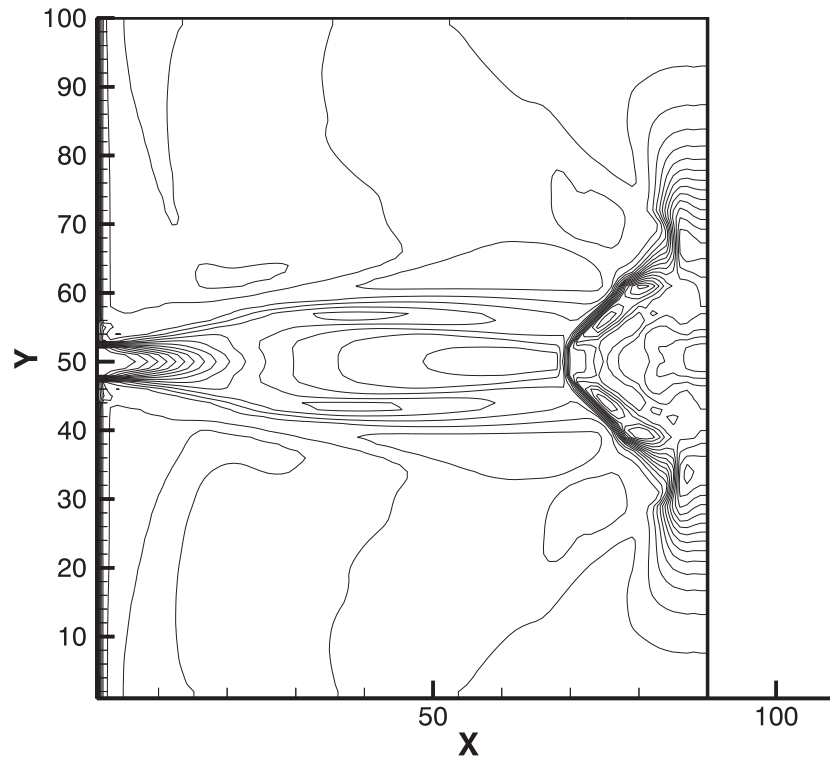Figure 12. Density isolines for the snapshot that corresponds to the separation stage.

Figure 13. Reconstructed density isolines for the snapshot from Figure 14.

It should be noted that the DMD results significantly depend on the number of snapshots. Figure 14 reveals the dependence of the error norm $\|r\|$ (Eq. (2)) on the number of snapshots N in a logarithmic scale for nonlinear mode. A convergence with increasing number of snapshots N is observable; however, when N exceeds some number, the convergence deteriorates.

Table I presents the relative computer time for different numbers of snapshots. For Intel Core2Duo CPU (3.0 GHz, 4.0 Gb), the necessary CPU time is small ($\sim 10^2$ s). However, the full scale problem ($N = Nt$, $Nt \sim 4 \cdot 10^4$) seems quite unsolvable both from memory (~ 100 Gb) and computer time (~ 3 months) considerations. In general, this result looks as very promising from the viewpoint of reduced-order approximation.
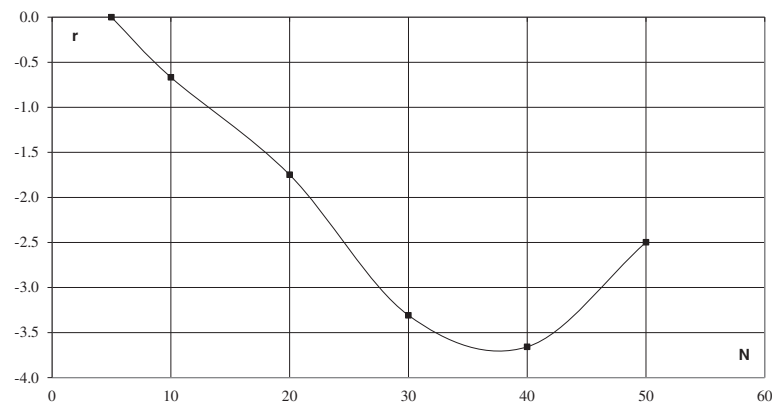

Figure 14. The logarithm of relative error norm $Log_{10}(\|r\|/\|r_0\|)$ (Eq. (2)) as function of the number of snapshots N.

Table I. The relative computer time as the number of snapshots.

N	10	20	30	40	50
t	1.0	2.71	3.47	4.73	5.76

5.2. DMD analysis of 2D shallow water dynamics

The shallow water equations have been used for a wide variety of hydrological and geophysical fluid dynamics phenomena such as tide currents [27], pollutant dispersion [28], storm surges, or tsunami wave propagation [29]. Early work on numerical methods for solving the shallow water equations is described in Navon (1979) [30]. The test problem used in this paper is consisting of the nonlinear shallow water equations model (also called the Saint Venant Equations [31]) in a channel on the rotating earth, associated with periodic boundary conditions in the $\widetilde{x}$-direction and solid wall boundary condition in the $\widetilde{y}$-direction:

$$\widetilde{u}_{\widetilde{t}} + \widetilde{u}\widetilde{u}_{\widetilde{x}} + \widetilde{v}\widetilde{u}_{\widetilde{y}} + \left(g\widetilde{h}\right)_{\widetilde{x}} - \widetilde{f}\,\widetilde{v} = 0, \tag{22}$$

$$\widetilde{v}_{\widetilde{t}} + \widetilde{u}\,\widetilde{v}_{\widetilde{x}} + \widetilde{v}\widetilde{v}_{\widetilde{y}} + \left(g\widetilde{h}\right)_{\widetilde{y}} + \widetilde{f}\,\widetilde{u} = 0, \tag{23}$$

$$\left(g\widetilde{h}\right)_{\widetilde{t}} + \left(g\widetilde{h}\widetilde{u}\right)_{\widetilde{x}} + (g\,\widetilde{h}\,\widetilde{v})_{\widetilde{y}} = 0, \tag{24}$$

$$\widetilde{u}(0,\widetilde{y},\widetilde{t}) = \widetilde{u}(L_{\max},\widetilde{y},\widetilde{t}), \quad \widetilde{v}(\widetilde{x},0,\widetilde{t}) = \widetilde{v}(\widetilde{x},D_{\max},\widetilde{t}) = 0, \tag{25}$$

where $\widetilde{u}$ and $\widetilde{y}$ are the velocity components in the $\widetilde{x}$ and $\widetilde{y}$ axis directions, respectively, $g\widetilde{h}$ is the geopotential height, $\widetilde{h}$ represents the depth of the fluid, $\widetilde{f}$ is the Coriolis factor, and g is the acceleration of gravity. Subscripts represent the derivatives with respect to time, and the streamwise and spanwise coordinate.

We consider that the reference computational configuration is the rectangular 2D domain $\Omega = [0, L_{\max}] \times [0, D_{\max}]$. We consider the model (22–25) in a β-plane assumption [32, 33], in which the effect of the Earth's sphericity is modeled by a linear variation in the Coriolis factor

$$\widetilde{f} = f_0 + \frac{\beta}{2}(2\widetilde{y} - D_{\max}), \tag{26}$$

where f_0 and β are constants and $L_{\max}$ and $D_{\max}$ are the dimensions of the rectangular domain of integration. The initial condition I1 introduced by Grammeltvedt [34] was adopted as the initial height field, which propagates the energy in wave number one, in the streamwise direction:

$$h_0(\widetilde{x},\widetilde{y}) = H_0 + H_1 \tanh\left(\frac{9(D_{\max}/2 - \widetilde{y})}{2D_{\max}}\right) + H_2 \sin\left(\frac{2\pi\widetilde{x}}{L_{\max}}\right)\cosh^{-2}\left(\frac{9(D_{\max}/2 - \widetilde{y})}{D_{\max}}\right). \tag{27}$$

Using the geostrophic relationship, $\widetilde{u} = -\widetilde{h}_{\widetilde{y}}\left(g/\widetilde{f}\right)$, $\widetilde{v} = \widetilde{h}_{\widetilde{x}}\left(g/\widetilde{f}\right)$, the initial velocity fields are derived as follows:

$$u_0(\widetilde{x},\widetilde{y}) = -\frac{g}{\widetilde{f}}\frac{9H_1}{2D_{\max}}\left(\tanh^2\left(\frac{9D_{\max}/2 - 9\widetilde{y}}{2D_{\max}}\right) - 1\right)$$
$$- \frac{18g}{\widetilde{f}}H_2\sinh\left(\frac{9D_{\max}/2 - 9\widetilde{y}}{D_{\max}}\right)\frac{\sin\left(\frac{2\pi\widetilde{x}}{L_{\max}}\right)}{D_{\max}\cosh^3\left(\frac{9D_{\max}/2 - 9\widetilde{y}}{D_{\max}}\right)}, \tag{28}$$

$$v_0(\widetilde{x},\widetilde{y}) = 2\pi H_2 \frac{g}{\widetilde{f}L_{\max}}\cos\left(\frac{2\pi\widetilde{x}}{L_{\max}}\right)\cosh^{-2}\left(\frac{9(D_{\max}/2 - \widetilde{y})}{D_{\max}}\right). \tag{29}$$

The dimensional constants used for the aforementioned model are

$$f_0 = 10^{-4}\text{s}^{-1}, \quad \beta = 1.5 \times 10^{-11}\text{s}^{-1}\text{m}^{-1}, \quad g = 10\text{ms}^{-1}, \tag{30}$$

$$D_{\max} = 44 \times 10^5\text{m}, \quad L_{\max} = 6 \times 10^6\text{m}, \quad H_0 = 2 \times 10^6\text{m}, \quad H_1 = 220\text{m}, \quad H_2 = 133\text{m}. \tag{31}$$

We have followed the approach used by Navon [32, 33], which implements a two-stage finite-element Numerov–Galerkin method for integrating the nonlinear shallow water equations on a β-plane limited-area domain, for approximating the quadratic nonlinear terms that appear in the equations of hydrological dynamics. We have captured a number of 240 unsteady solutions of the 2D shallow water equations model (22–25), with the time step $\Delta t = 600$s.

To measure the accuracy of the reduced shallow water model and to validate the numerical results with existing results in the literature, we undertake a non-dimensional analysis of the shallow water model. Following [35], reference quantities of the dependent and independent variables in the shallow water model are considered, that is, the length scale $L_{ref} = L_{\max}$ and the reference units for the height and velocity, respectively, are given by the initial conditions $h_{ref} = h_0$, $u_{ref} = u_0$. A typical time scale is also considered, assuming the form $t_{ref} = L_{ref}/u_{ref}$. In order to make the system of equations (22–25) non-dimensional, we define the non-dimensional variables $(t, x, y) = (\tilde{t}/t_{ref}, \tilde{x}/L_{ref}, \tilde{y}/L_{ref})$, $(h, u, v) = (\tilde{h}/h_{ref}, \tilde{u}/u_{ref}, \tilde{v}/u_{ref})$. The numerical results are obtained and used in further numerical experiments in dimensionless form.

In this section, the application of DMD based on the reduced Schmid operator [1] is illustrated by comparing the evolution of the flow field along the integration time window in the cases of the full model and the reduced-order model. The DMD spectra for the $(h, u, v)(x, y, t)$ fields are presented in Figure 15. The DMD technique presented herein is fully capable of determining the modal growth rates and the associated frequencies, which are illustrated in Figure 16, for geopotential height field h.

Figure 17 presents the isolines of first right eigenvector and isolines of the first left eigenvector of the reduced Schmid operator, for the $(h, u, v)(x, y, t)$ fields. We perform the reconstruction of the
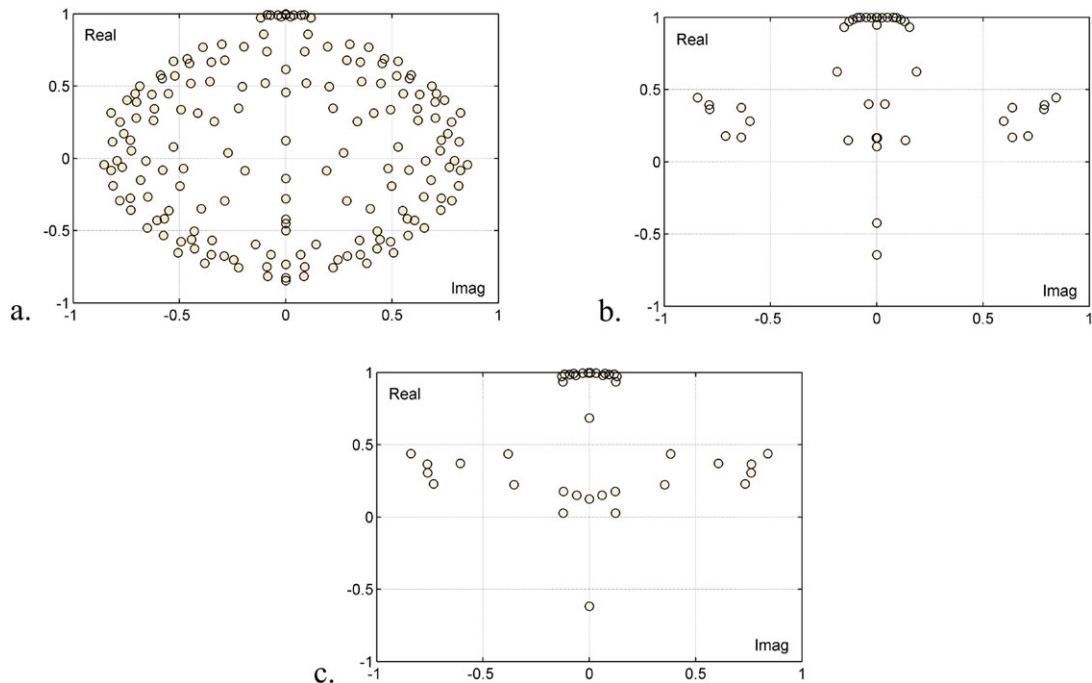

Figure 15. Spectrum of dynamic mode decomposition $\lambda_{\text{Re}}(\lambda_{\text{Im}})$ for (a) geopotential height field h, (b) streamwise velocity field u, and (c) spanwise velocity field v.
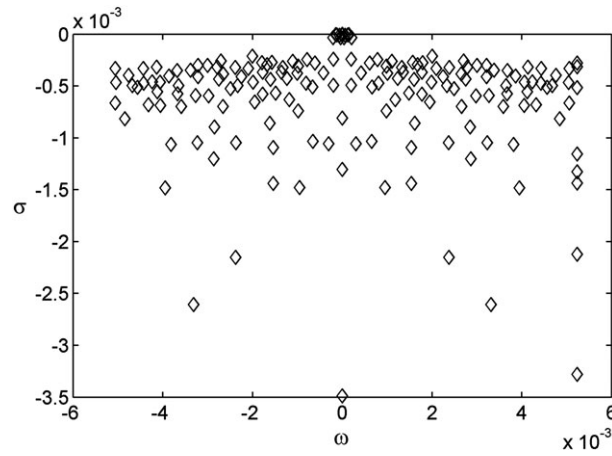
Figure 16. Growth rates and associated frequencies (σ, ω) obtained by dynamic mode decomposition of the geopotential height field h.
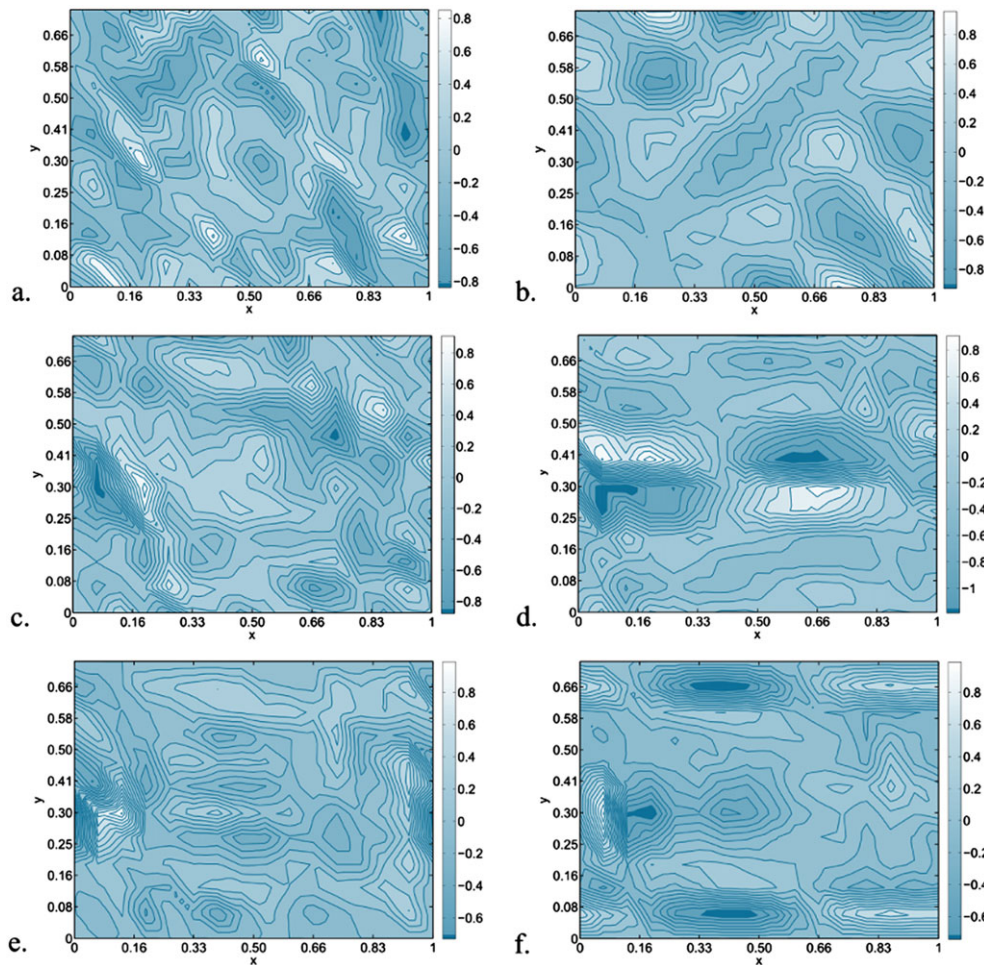

Figure 17. Isolines of the real left eigenvector (a, c, and e) and isolines of the real right eigenvector (b, d, and f) of the reduced Schmid operator, obtained by dynamic mode decomposition of the h, u, and v fields, respectively.

$(h, u, v)(x, y, t)$ fields after 200 steps, in Figure 18. We applied a normalization condition such that the maximum amplitude of the physical components $(h, u, v)(x, y, t)$ fields over the (x, y) stations is unity.

In the case of DMD algorithm employed in [2, 6], the number of stored modes was 192, 180, and 151, respectively. The DMD algorithm based on the reduced Schmid operator leads to a number of 173 modes retained for the reconstruction of geopotential height field, 42 modes retained for the reconstruction of the streamwise velocity field, and 40 modes retained for the reconstruction of the spanwise velocity field; thus, a significant reduction in computational storage is achieved.

Selection of dynamic modes and amplitudes used for the flow reconstruction constitutes the source of many discussions among modal decomposition practitioners [3, 6, 36]. The superposition of all dynamic modes, weighted by their amplitudes and complex frequencies, approximates the entire data sequence, but there are also modes that have a weak contribution. On the other hand, the non-orthogonality of dynamic modes may raise the projection error while increasing the order of the DMD basis.

To avoid these difficulties, we introduce in the following a numerical procedure to optimize the selection of dynamic modes involved in developing of a reduced-order model of the flow. Assuming that, for the problem investigated here, there are no modes that are very rapidly damped having very high amplitudes, we explore the selection of the modes based on sorting them in decreasing
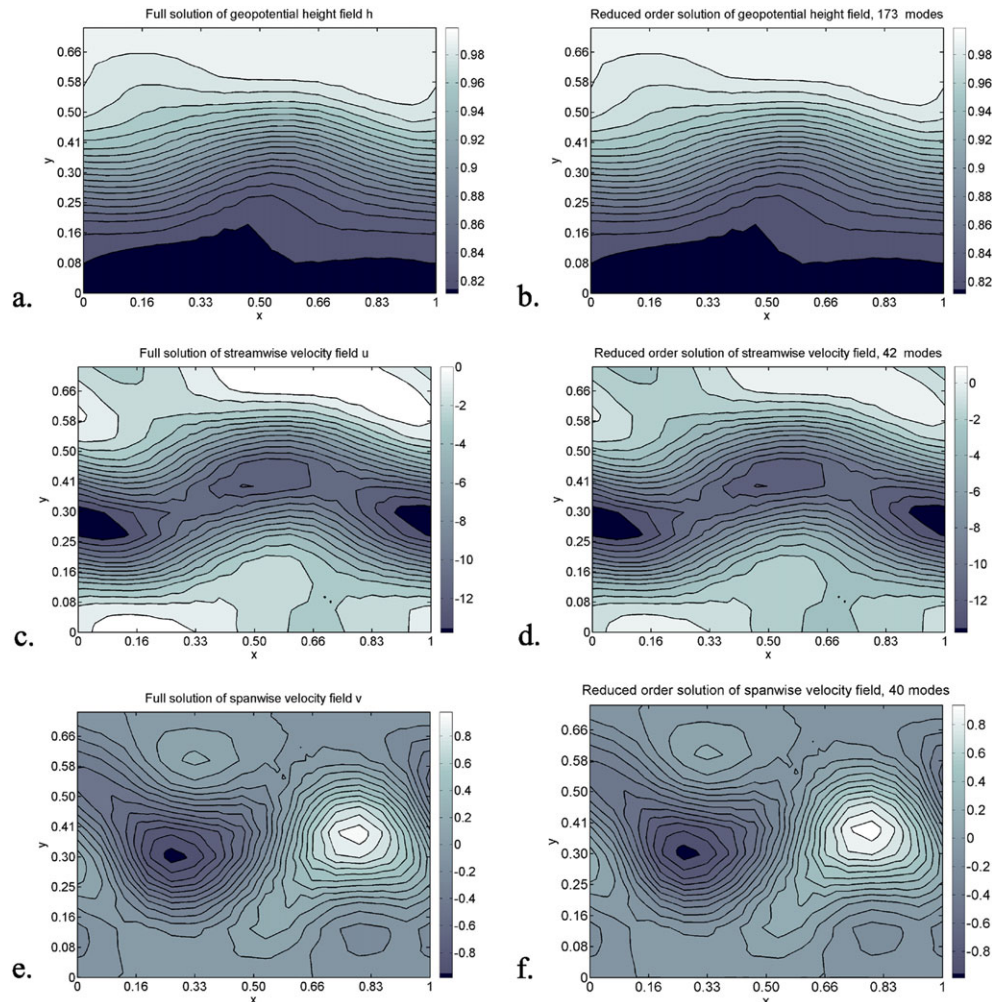

Figure 18. Full solution of *h*, *u*, and *v* fields (a, c, and e) versus reconstruction of *h*, *u*, and *v* fields, respectively (b, d, and f), employing the dynamic mode decomposition based on reduced Schmid operator, after 200 steps.

order of their amplitudes. Based on the method of reduced Schmid operator presented herein, we retain dynamic modes and associated frequencies in descending order of their amplitudes until a minimum relative error of reconstruction is achieved.

We define the relative error as the L_2-norm of the difference between the variables of the full shallow water equation model and approximate DMD solutions over the exact one, that is,

$$Er_{DMD} = \frac{\|w(x,y) - w_{DMD}(x,y)\|_2}{\|w(x,y)\|_2}, \tag{32}$$

where $w(x,y) \equiv (h, u, v)(x, y)$ represent the full solution of the shallow water equation model and $w_{DMD}(x,y) \equiv (h_{DMD}, u_{DMD}, v_{DMD})(x, y)$ represent the solution obtained by employing the optimized DMD based on the reduced Schmid operator.

We defer to a future study the investigation of other different techniques for identification of an optimal truncated representation of the flow field in order to capture the most important dynamic structures. The amplitudes of the optimized DMD modes function of the estimated frequencies, for $h, u,$ and v fields, respectively, are illustrated in Figure 19, where diamonds represent the retained modes, while circles represent discarded modes after DMD optimization. After the optimized DMD is applied, the representation of the flow field is achieved, retaining 19 modes for geopotential height field h, 28 modes for streamwise velocity field u, and 33 modes for spanwise velocity field v.

The relative error computed as the retained number of dynamic modes is depicted in Figure 20. A comparison of the retained number of dynamic modes, in the case of classical DMD, DMD based on the reduced Schmid operator proposed in this paper and the optimized number of retained modes is presented in Table II. A significant reduction of a factor of 10 is achieved for the representation of
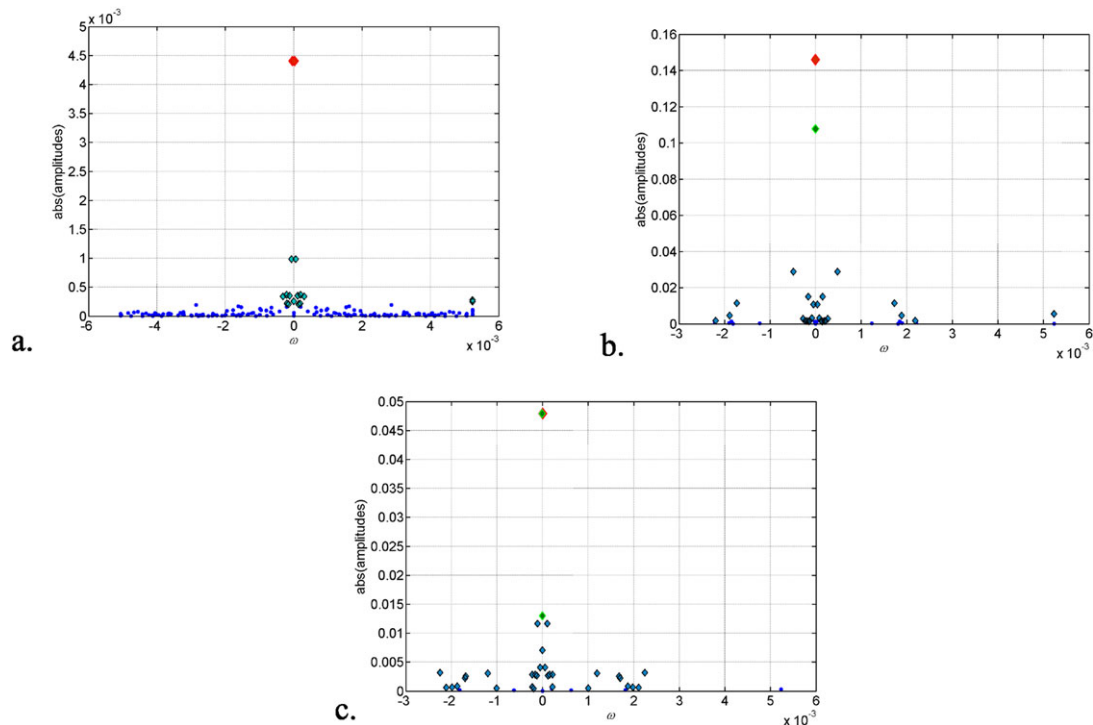

Figure 19. The amplitudes of the dynamic mode decomposition (DMD) modes as the estimated frequencies, for h, u, and v fields, respectively, case of DMD based on the reduced Schmid operator. Diamonds represent retained modes after DMD optimization, while circles represent discarded modes.
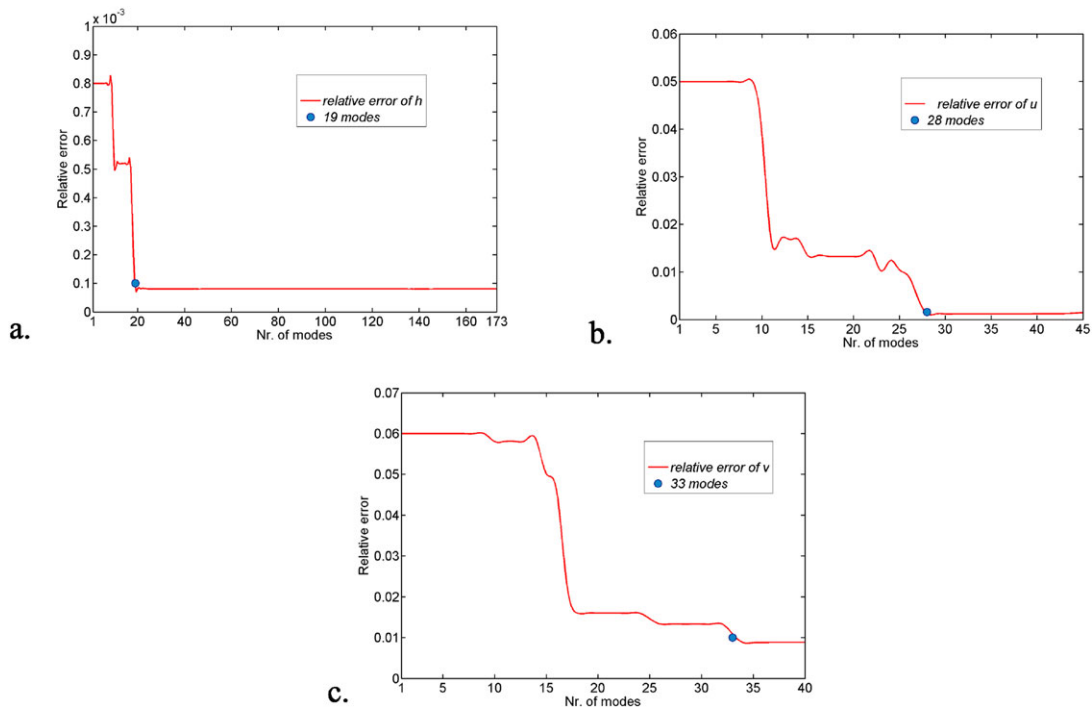
Figure 20. The relative error computed as the retained number of dynamic modes, in case of optimized dynamic mode decomposition based on the reduced Schmid operator, for h, u, and v fields, respectively.

Table II. The number of retained modes and relative error obtained by employing the optimized DMD based on the reduced Schmid operator.

Flow field	DMD method [2, 6]	DMD based on reduced Schmid operator [1]	Optimized DMD based on reduced Schmid operator	Relative error Er_{DMD}
$h(x, y)$	192	173	19	0.0002683
$u(x, y)$	180	42	28	0.0016223
$v(x, y)$	151	40	33	0.0120628

geopotential height field, while the representation of the velocity field is improved by a factor of one and a half in computational resources.

The improved DMD approach introduced in this paper has been validated by comparing our results with those obtained by Stefanescu and Navon [37], when an alternating direction fully implicit finite-difference scheme was used for discretization of 2D shallow water equations on a β-plane, and the proper orthogonal decomposition (POD) coupled with discrete empirical interpolation was employed for the model reduction. In [37], the dimensions of POD bases for each variable was taken to be 35, while in the optimized DMD in the present approach, we involve a smaller number of dynamic modes (Table II). The flow reconstructions presented in Figure 21 are very close to those computed in [37], comparing the solution of flow field after 79 steps. The relative error obtained by employing the optimized DMD based on the reduced Schmid operator in reconstruction of the flow fields is presented also in Table II.

The similarity between these characteristics of the flow field and those obtained in the previous investigation validates the method presented here and certifies that the improved DMD method can be applied successfully to model reduction of 2D flows.

6. SOME FEASIBLE APPLICATIONS OF THE SCHMID OPERATOR

The reduced form of the Schmid operator promises certain prospects in a set of additional applications.
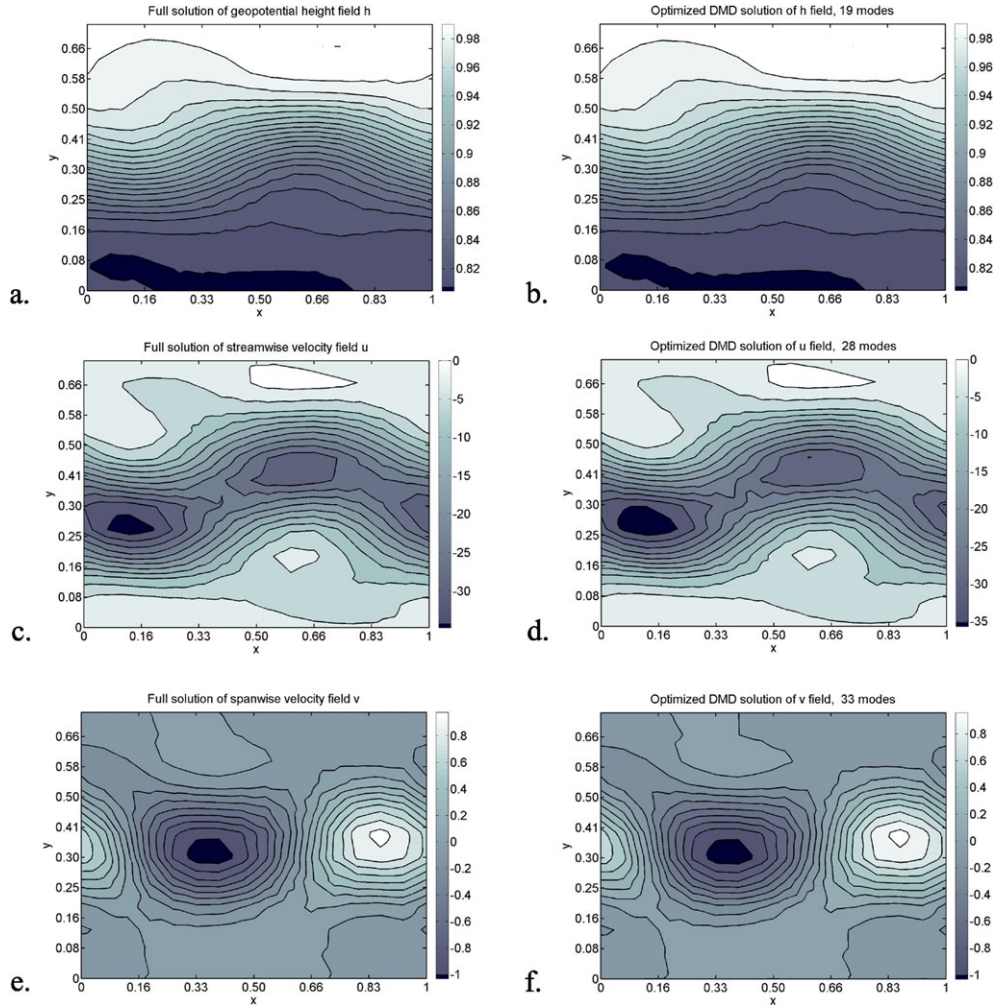
Figure 21. Reconstruction of *h*, *u*, and *v* fields, respectively, employing the optimized dynamic mode decomposition based on reduced Schmid operator, after 79 steps. A significant reduction in the number of retained dynamic modes is achieved compared with numerical results in [37].

6.1. Singular vectors

Disturbances, maximally growing for certain time interval, may be related to the eigenvectors of the operator composed of the product of forward and adjoint propagators [16].

The equation $du/dt = Bu$ in the linear approach may be resolved by the operator

$$u(\Delta t) = e^{B\Delta t}u_1 = Lu_1 \tag{33}$$

The norm of the solution assumes the form

$$\|u(\Delta t)\| = (Lu_1, Lu_1) = (u_1, L^*Lu_1) \tag{34}$$

The search for maximally growing linear perturbations $\|u(\Delta t)\|/\|u_1\|$ at time interval Δt reduces to the search of eigenvectors $L^{*E}L\eta_{\max} = \sigma^2_{\max}\eta_{\max}$ with the maximum eigenvalue $\sigma^2_{\max}$. The problem may be resolved iteratively using the action of the operator $A*A$.

For a small enough time interval between snapshots, the Schmid operator is linear, which provides an opportunity for the calculation of singular vectors.
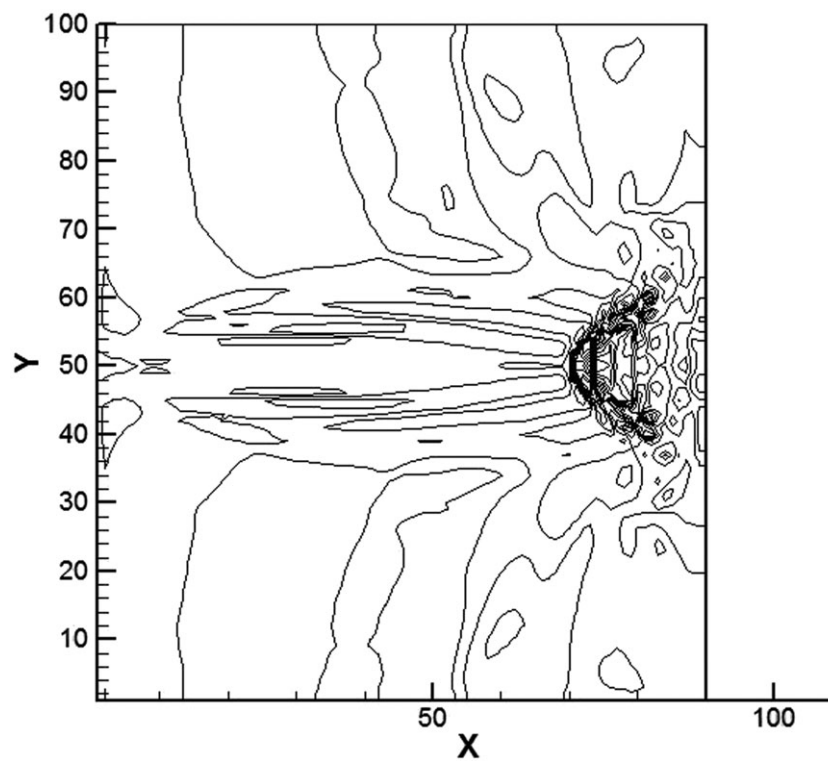
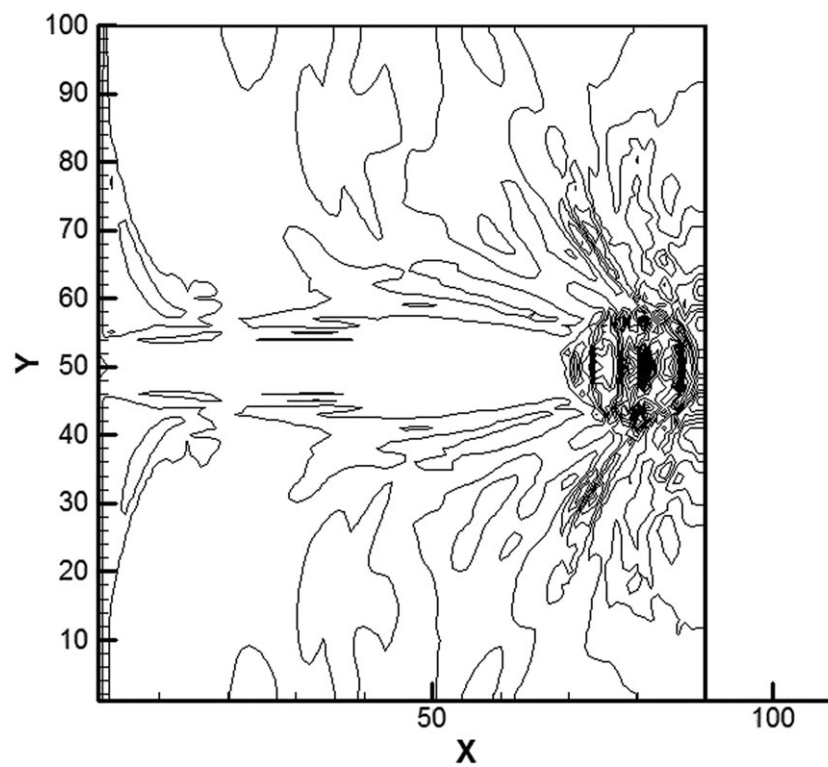Figure 22. Isolines of singular vector (density component) in linear mode.

Figure 23. Isolines of singular vector (density component) in nonlinear mode.

Figure 22 presents the singular vector for the impinging jet linear mode (the distance between snapshots (in steps) $k = 10$, $\sigma_{max} = 1.82$); Figure 23 presents the similar vector for the nonlinear mode ($k = 500$, $\sigma_{max} = 2.45$).

Both the magnitude of eigenvalues and the shape of the eigenvectors (singular vectors) are quite different in the cases of linear and nonlinear events, respectively.

6.2. Receptivity

Eigenvectors of forward $A_{ji}(\Delta t)$ and adjoint propagators $A_{ij}^*(\Delta t)$ (Ω_R and Ω_L, correspondingly) are biorthogonal, which is important for the estimation of the flow receptivity to perturbations. It is known [15] that an initial disturbance should correspond to k-th mode of adjoint problem (Ω_L) in order to maximally excite the k-th mode of the forward problem. Thus, if right eigenvectors (dynamic modes) are useful at the search of main flow features, the left eigenvectors determine a receptivity of the flow to the external action.

The availability of left eigenvectors Ω_L enables estimation of the flow receptivity to initial field disturbances without applying an especial adjoint solver, such as those used in Refs [15] and [16].

7. CONCLUSION

In this paper, we have proposed a new framework for DMD. The key innovation resides in application of the reduced Schmid operator instead of the classic DMD approach.

We proved that the DMD is equivalent to the Schmid operator approximation by a product of rectangular matrices of the right eigenvectors (dynamic modes), the left eigenvectors, and the eigenvalue matrix. Instead of storing the total operator matrix, the proposed technique enables storing only two rectangular matrices and one diagonal matrix, which ensures computer memory and computing time (CPU) savings of about several orders of magnitude.

Extending the results from [1], the main findings of our investigation are summarized in the following:

- the Schmid operator, on the same solution, may have either linear or nonlinear forms, in dependence on the time interval between snapshots; and
- the Schmid operator in the linear limit may be of interest from the viewpoint of the estimation of receptivity and singular vectors.

In order to assess the performances of the proposed method, we have considered two numerical test experiments: the case of a 2D supersonic underexpanded jet on a plate and the problem of the 2D shallow water equations. We applied the proposed DMD algorithm based on the reduced Schmid operator for different snapshots obtained by sampling down the original solutions of the full model with different time steps. We compared the novel DMD approach with the classic one in both cases.

Based on the DMD method introduced in [1], we proposed the optimization of DMD algorithm for reducing the number of dynamic modes retained for reconstructing the flow field. We arrange the modes in descending order of their amplitudes, and we retain only the number of modes necessary for flow reconstruction with a minimum relative error. This procedure works well for models without modes that are very rapidly damped, having very high amplitudes. In these cases, different methods for retaining the modes shall be imposed, and we defer this discussion to a future study.

We emphasized the excellent behavior of the proposed optimized DMD method compared with the POD-based model recent results existing in the literature [37]. Moreover, the model reduction technique proposed in this paper leads to a significant reduction in the number of retained modes, in comparison with the existing techniques. Additionally, we presented a rigorous error analysis for the reduced-order models, and we compared the relative computational efficiency of the aforementioned DMD technique.

ACKNOWLEDGEMENTS

REFERENCES

1. Schmid PJ. Dynamic mode decomposition of numerical and experimental data. *Journal of Fluid Mechanics* 2010; **656**(1):5–28.
2. Rowley CW, Mezic I, Bagheri S, Schlatter P, Henningson DS. Spectral analysis of nonlinear flows. *Journal of Fluid Mechanics* 2009; **641**:115–127.
3. Chen KK, Tu JH, Rowley CW. Variants of dynamic mode decomposition: boundary condition, Koopman, and Fourier analyses. *Journal of Nonlinear Science* 2012; **22**:887–915.
4. Guéniat F, Mathelin L, Pastur LR. A dynamic mode decomposition approach for large and arbitrarily sampled systems. *Physics of Fluids* 2015; **27**:025113.
5. Jovanovic MR, Schmid PJ, Nichols JW. Sparsity-promoting dynamic mode decomposition. *Physics of Fluids* 2014; **26**:024103.
6. Bistrian DA, Navon IM. An improved algorithm for the shallow water equations model reduction: dynamic mode decomposition vs POD. *International Journal for Numerical Methods in Fluids* 2015; **79**(9):552–580.
7. Holmes P, Lumley JL, Berkooz G. *Turbulence, Coherent Structures, Dynamical Systems and Symmetry*. Cambridge Univ. Press: New York, 1996.
8. Bagheri S. Koopman-mode decomposition of the cylinder wake. *Journal of Fluid Mechanics* 2013; **726**:596–623.
9. Mezic I. Analysis of fluid flows via spectral properties of the Koopman operator. *Annual Review of Fluid Mechanics* 2013; **45**(1):357–378.
10. Tu JH, Rowley CW, Luchtenburg DM, Brunton SL, Kutz JN. On dynamic mode decomposition: theory and applications. *Journal of Computational Dynamics* 2014; **1**(2):391–421.
11. Hemati MS, Williams MO, Rowley CW. Dynamic mode decomposition for large and streaming datasets. *Physics of Fluids* 2014; **26**:111701. doi:10.1063/1.4901016.
12. Williams MO, Rowley CW, Mezic I, Kevrekidis IG. Data fusion via intrinsic dynamic variables: an application of data-driven Koopman spectral analysis. *EPL (Europhysics Letters)* 2015; **109**(4):40007. doi:10.1209/0295-5075/109/40007.
13. Koopman B. Hamiltonian systems and transformations in Hilbert space. *Proceedings of the National Academy of Sciences of the United States of America* 1931; **17**:315–318.
14. Lan YH, Mezic I. Linearization in the large of nonlinear systems and Koopman operator spectrum. *Physica D-nonlinear Phenomena* 2013; **242**:42–53.
15. Hill DC. Adjoint systems and role in the receptivity problem for boundary layers. *Journal of Fluid Mechanics* 1995; **292**:183–204.
16. Farrell BF, Moore AM. An adjoint method for obtaining the most rapidly growing perturbation to oceanic flows. *Journal of Physical Oceanography* 1992; **22**:338–349.
17. Golub GH, Van Loan CF. *Matrix Computations*. JHU Press: Baltimore, Maryland, USA, 1996.
18. Magnus W. On the exponential solution of differential equations for a linear operator. *Communications on Pure and Applied Mathematics* 1954; **VII**:649–673.
19. Blanes S, Casas F, Oteo JA, Ros J. The Magnus expansion and some of its applications. *Physics Reports* 2009; **470**:151–238.
20. Casas F, Iserles A. Explicit Magnus expansions for nonlinear equations. *Journal of Physics A: Mathematical and General* 2006; **39**:5445–5461.
21. Kaiser E, Noack BR, Cordier L, Spohn A, Segond M, Abel M, Daviller G, Östh J, Krajnović S, Niven RK. Cluster-based reduced-order modelling of a mixing layer. *Journal of Fluid Mechanics* 2014; **754**:365–414.
22. Anderson E, Bai Z, Bischof C, Blackford S, Demmel J, Dongarra J, Du Croz J, Greenbaum A, Hammarling S, McKenney A, Sorensen D. *LAPACK Users' Guide* (3rd edn). SIAM: Philadelphia, 1999.
23. Lehoucq RB, Sorensen DC, Yang C. *ARPACK Users Guide: Solution of Large-scale Eigenvalue Problems with Implicitly Restarted Arnoldi Methods*. SIAM: Philadelphia, 1998.
24. Pundir B, Dhanak M. Surface pressure fluctuations due to an impinging supersonic underexpanded jet. *AIAA* 2010; **107**:1–13.
25. van Leer B. Towards the ultimate conservative difference scheme. V. A second-order sequel to Godunov's method. *Journal of Computational Physics* 1979; **32**:101–136.
26. Sun M, Katayama K. An artificially upstream flux vector splitting for the Euler equations. *Journal of Computational Physics* 2003; **189**:305–329.
27. Bryden IG, Couch SJ, Owen A, Melville G. Tidal current resource assessment. *Proceedings of the IMechE, Part A: Journal of Power and Energy* 2007; **221**:125–135.

28. Sportisse B, Djouad R. Reduction of chemical kinetics in air pollution modeling. *Journal of Computational Physics* 2000; **164**:354–376.
29. Koutitus C. *Mathematics Models in Coastal Engineering*. Pentech Press: London, 1988.
30. Navon IM. Numerical methods for the solution of the shallow-water equations in meteorology. University of the Witwatersrand, Johannesburg (South Africa), PhD Thesis, available from ProQuest, UMI Dissertations Publishing, 1979. 0533651.
31. Vreugdenhil CB. *Numerical Methods for Shallow Water Flow*. Kluwer Academic Publishers, 1994.
32. Navon IM. A Numerov–Galerkin technique applied to a finite-element shallow water equations model with enforced conservation of integral invariants and selective lumping. *Journal of Computational Physics* 1983; **52**:313–339.
33. Navon IM. FEUDX: a two-stage, high accuracy, finite-element FORTRAN program for solving shallow-water equations. *Computers and Geosciences* 1987; **13**(3):255–285.
34. Grammeltvedt A. A survey of finite-difference schemes for the primitive equations for a barotropic fluid. *Monthly Weather Review* 1969; **97**(5):384–404.
35. Barenblatt GI. *Scaling, Self-similarity, and Intermediate Asymptotics. Cambridge Texts in Applied Mathematics*. Cambridge University Press: Cambridge, New York, Melbourne, 1996.
36. Jovanovic MR, Schmid PJ, Nichols JW. Low-rank and sparse dynamic mode decomposition. *Center for Turbulence Research Annual Research Briefs* 2012; **2012**:139–152.
37. Stefanescu R, Navon IM. POD/DEIM nonlinear model order reduction of an ADI implicit shallow water equations model. *Journal of Computational Physics* 2013; **237**:95–114.